Desalination and Water Treatment 320 (2024) 100771

Contents lists available at ScienceDirect

Desalination and Water Treatment

journal homepage: www.sciencedirect.com/journal/desalination-and-water-treatment/

Adsorption of nickel (II) from aqueous solutions with clay-supported nano-scale zero-valent iron synthesized from green tea extract

Armand Tchakounte [a,*], Charles Kede [a,b], Victor Shikuku [c,*], Idriss Lenou [a], Joseph Dika [a]

[a] Department of Chemistry, Faculty of Science, University of Douala, P.O. Box 24175, Douala, Cameroon
[b] Department of Process Engineering, National Higher Polytechnic School of Douala, University of Douala, P.O. Box 2701, Douala, Cameroon
[c] Department of Physical Sciences, Kaimosi Friends University, P.O. Box 385-50309, Kaimosi, Kenya

GRAPHICAL ABSTRACT

ARTICLE INFO

Keywords:
Green tea
Incorporation
Clay
Kinetics study
Surface chemistry

ABSTRACT

Nano zerovalent iron (nZVI) supported adsorbents have been reported as suitable candidates for adsorption of water contaminants. However, the role of and interplay between surface chemistry, functional group density and textural properties has largely been unexplored. In this work, green tea derived nano zerovalent iron (nZVI) supported clay hybrid material (CnZVI) was used as a novel adsorbent for the removal of Ni^{2+} ions from water. The unmodified natural clay (Arg) and the CnZVI composite were characterized using FTIR, SEM, TGA and BET techniques. Incorporation of nZVI ameliorated the specific surface area from 16.88 to 30.46 m^2/g, translating to ~80 % increase. This translated to ~69 % increase in maximum adsorption capacity from 8.47 to 14.38 mg/g, respectively. The addition of nZVI in the clay decreased the affinity (K_F) for Ni^{2+} by ~48 %. The disparity between the percent increase in surface area (~80 %) and the adsorption capacity (~69 %) implies the adsorption of Ni^{2+} was significantly controlled by textural properties compensating for the antagonistic effects of functional group density. The kinetic rates were best predicted by the pseudo-first-order and Elovich's models for the Arg and CnZVI, respectively, implicit evidence of the role of surface chemistry. A maximum adsorption capacity of 14 mg/g was achieved for 100 mg Ni^{2+}/L in 120 min for CnZVI.

* Corresponding authors.
E-mail addresses: armanduchiwa@gmail.com (A. Tchakounte), vshikuku@kafu.ac.ke (V. Shikuku).

https://doi.org/10.1016/j.dwt.2024.100771
Received 27 May 2024; Received in revised form 29 August 2024; Accepted 10 September 2024
Available online 13 September 2024

1. Introduction

Heavy metals (HMs) account for a major quantity of contaminants found in wastewater spawned by a large variety of industries. These heavy metal ions present a risk to the environment because of the growing noxious and non-biodegradability impacts they have [1]. Above certain concentrations, heavy metals such as nickel are toxic to human beings causing dermatitis, allergies, kidney disturbances, cancer of lungs, nose and bone among other disorders [2]. Nickel has extensive use in various inventions and procedures. Some of its uses are in industrial processes like coating, to produce batteries quarrying, metal finishing, porcelain coating and tint productions [3]. The allowable limit standard for nickel set by the US EPA in wastewater for short-term effluent is 2 mgL^{-1} and 0.2 mgL^{-1} for long-term effluent for reuse [4].

Therefore, it becomes important to eliminate nickel and other toxic heavy metals from effluents [5]. Available methods for heavy metals removal from water include; filtration, membrane processes, complexation, chemical precipitation, reverse osmosis, evaporation, coagulation, chemical redox, ion exchange and solvent extraction [3,6,7]. However, these methods have several disadvantages, such as incomplete removal of metals, excessive use of reagent and energy, low selectivity, capital intensive and the production of toxic by-products. Consequently, new, more economical methods for the removal of heavy metals from industrial effluents have emerged, such as simple, more technically feasible adsorption, with greater efficiency in the removal of heavy metals from suspensions.

With the advancement of nanotechnology, nanoscale zero-valence iron (nZVI) has been studied and used for heavy metal removal considering the tremendously tiny particle size, large surface area and high reactivity [8]. The adsorption mechanisms were shown to be controlled by the identity the heavy metal and its thermodynamic properties. These nanoparticles (nZVI) have numerous applications in various environmental fields such as the remediation of soils, sediments and water [4,9]. Various chemical and physical methods were reported for synthesis of nZVI. However, the downside of these methods is that they are very expensive, requiring unique equipment, energy-intensive and consume toxic chemicals such as sodium borohydride ($NaBH_4$) [10]. The implementation of simple, economical and environmentally friendly methods, aligned with the principles of green chemistry, for the synthesis of nZVI are necessary. Thus, the environmentally friendly production of nZVI with plant extracts such as eucalyptus leaves has been highlighted [11]. Plants extracts act as reducing and binding agents owing to their antioxidant composition such as polyphenols, reducing sugars, nitrogenous bases and amino acids [11]. However, nZVI also suffers other limitations such as oxidation that reduce reactivity and, agglomeration reducing dispersivity in aqueous solution resulting to low performance. These can be partly overcome by use of a suitable support material to immobilize the nZVI particles [12].

Clay minerals have different adsorption capacities for metal ions [13,14]. They have distinct properties such as large surface areas, high cation exchange capacity (CEC), abundance even in remote localities, which makes them suitable for hosting nZVI [12].

However, the effect of the clay, synergistic or antagonistic, as a support material depends on the type of clay, crystal structure and composition. Since there is paucity of data of data on the role of clays as support materials, additional studies on clay-nZVI are need to better our understanding and shed light on the selection of clays as support materials. Furthermore, the role of surface chemistry and textural properties of nZVI coated materials has been largely unexplored. The main objective of this study was to study the performance of nZVI, derived from green tea leaves, supported on a natural clay material for the adsorption of Ni^{2+} ions from aqueous solution. The synergistic or antagonistic effect, on textural, surface functionality and adsorptive performance, was determined by comparison with unmodified clay (Arg).

2. Materials and methods

2.1. Materials

The ferrous sulfate heptahydrate ($FeSO_4.7\ H_2O$), sodium hydroxide (NaOH) and sulfuric acid (H_2SO_4) were of analytical grade. Marketable green tea leaves were used as sources of polyphenols. The clay samples were collected from a subtropical wetland soil in Cameroon (Littoral Region), Central Africa. The elemental composition (%) in terms of bulk oxides of the unmodified clay sample from XRF analysis was as follows: SiO_2: 68.23, Al_2O_3: 13.57, Fe_2O_3: 6.60, K_2O: 0.44, MgO: 0.44, CaO: 0.68 and Na_2O: 0.21.

2.2. Synthesis of CnZVI

Preparation protocol for the CnZVI is in accordance with the method reported by [15]. A 20 g sample of green tea leaves was heated until 80 °C in 1 L deionized water and sieved with the aid of vacuum filtration. A 50 mL of 0.1 M Fe^{2+} solution was added to 75 g of clay. To this mixture, the tea extract was added at a ratio of 1:2 (v/v) while stirring at room temperature for 30 min. The adsorbent obtained, nZVI-loaded clay (CnZVI), after filtration was washed with ethylene to remove the remaining excess ferrous sulfate heptahydrate and then oven-dried for 24 h..

2.3. Characterization of unmodified clay (Arg) and CnZVI

The specific surface areas of the sorbents were obtained by N_2 adsorption-desorption method using the BET isotherm equation [16]. The porous properties of unmodified clay (Arg) and CnZVI were determined by nitrogen adsorption at 77.35 K with a micrometrics ASAP-2010 automatic volumetric sorption analyzer, as described in reference [17]. The pH drift technique [18,19] was used to determine the pH_{pzc} value for the adsorbents. TGA analysis was performed for natural clay (Arg) and nZVI coated clay (CnZVI) samples to determine their thermal stability. The surface functional groups were inspected using the FT-IR spectroscopy (Brucker Vector-22, Germany). A scanning electron microscope (Philip XL30/EDX, Germany) provided micrographs scans for the adsorbents.

2.4. Batch adsorption

Batch adsorption was performed to evaluate the effect of process parameters on the adsorption of Ni^{2+} ions from the aqueous solution using the natural clay (Arg) and CnZVI. A 100 mL solution of Ni^{2+}ion with different concentrations (10–100 mgL^{-1}), sorbent doses (0.2 g), and stirring time (5–120 min) were added to 200 mL Erlenmeyer flasks and the mixtures stirred until pseudo-equilibrium was attained at 120 min. The residual Ni^{2+}ions in the solution was determined using an atomic adsorption spectrophotometer (AAS) (Spectroquant Pharo 300, Japan). The amount of nickel uptake at equilibrium (Qe) was determined using the following equation.

$$Q_e = \frac{(C_0 - C_e) \times V}{m} \quad (1)$$

With C_0 and C_e as the initial and equilibrium concentrations of Ni^{2+} ions (mgL^{-1}), respectively, V is the volume of solution (L) and m is the amount of adsorbent (g).

2.5. Adsorption kinetic study

To understand the adsorption mechanism, the experimental data were fitted to the pseudo-first order (PFO) [20], pseudo-second order (PSO) [21] and Elovich kinetic models [22]. The PFO model postulates a physical adsorption between the sorbent and the sorbate [23,24]. It is represted by Eq. 2:

$$Q_t = q_e(1 - \exp(-k_1 t)) \quad (2)$$

Where Q_t (mgg^{-1}) the amount adsorbed at any time, q_e (mgg^{-1}) amount adsorbed at equilibrium, k_1 the PFO kinetic rate constant (min^{-1}) and t is time (min).

The PSO model postulates a chemical interaction between both sorbent and sorbate as predominating mechanism. The model is given by Eq. 3 [21]:

$$Q_t = \frac{q_e^2 k_2 t}{1 + q_e k_2 t} \quad (3)$$

Where k_2 ($g.mg^{-1}min^{-1}$) PSO rate constant. The other parameters are as previously defined.

Elovich kinetic model is represented as follows [22]:

$$Q_t = (1+\beta)\ln(1+\alpha\beta t) \quad (4)$$

With β representing the desorption constant linked to the activation energy of chemisorption ($g^{-1}mg$) and α is the initial adsorption rate (mg/(g.min)).

2.6. Isothermal study

Mostly, the goodness of adsorption largely relies on the equilibrium between solid and liquid phases. Two parameters isotherm models were used to describe the Ni^{2+} ions uptake upon the selected sorbent such as Langmuir, Freundlich and Dubinin-Radushkevich (D-R).

The Langmuir isotherm is assumes a monolayer adsorption on an energetically homogenous surface [25]. The equation below gives the expression of Langmuir isotherm model:

$$Q_e = \frac{q_m b C_e}{1 + b C_e} \quad (5)$$

Where Q_e (mgg^{-1}) the equilibrium adsorption capacity, C_e (mgL^{-1}) the residual Ni^{2+} concentration at equilibrium concentration and q_m and b denote the theoretical maximum monolayer adsorption density (mg.g^{-1}) and the Langmuir constant ($L.g^{-1}$), respectively.

Freundlich isotherm model is represented in Eq. 6 [26]:

$$Q_e = K_F C_e^{1/n} \quad (6)$$

Where C_e (mgL^{-1}) the metal ions concentration at equilibrium, K_F the Freundlich affinity factor constant (mgg^{-1})(Lmg^{-1})$^{1/n}$ and n describes the favorability of the adsorption reaction.

The mean free energy factor of the Dubinin-Radushkevitch (D-R) model provides insight on the operative mechanism of the adsorption process, whether it is physical or chemical. The D-R isotherm equation is given in Eq. 7 [27]:

$$q = q_{D-R}\exp(-\beta\varepsilon^2) \quad (7)$$

Where q_{D-R} is the maximum adsorption capacity (mgg^{-1}), β the activity coefficient linked to the sorption free energy ($mol^2.kJ^{-2}$), and ϵ the Polanyi potential, defined by Eq. (9).

$$\varepsilon = RT\ln\left(1 + \frac{1}{C_e}\right) \quad (8)$$

The mean adsorption energy E_a (KJ/mol), Eq. 10, is an index of the adsorption mechanism and is valuable in distinguishing physisorption and chemisorption phenomena.

$$E_a = \frac{1}{\sqrt{2\beta}} \quad (9)$$

3. Results and discussions

3.1. Adsorbent characterization

The Textural properties, surface area, total pore volume, average pore diameter, pH_{zpc} and pore size distribution are presented in Table 1. The incorporation of nZVI increased the surface area (SA) from 16.88 to 30.46 $m^2.g^{-1}$ for Arg and CnZVI, respectively. This is possibly due to intercalation of nZVI in the clay layers [28]. Similar results have been

Table 1
Adsorbent textural characterizations.

	Arg	CnZVI
Density ($g.cm^{-3}$)	1.00	1.00
BET total Surface area ($m^2.g^{-1}$)	16.88	30.46
Total pore volume ($cm^3.g^{-1}$)	0.11	0.28
Nanoparticule size (Å)	4148.85	3555.44
Average pore diameter	17.54 Å	27.9 Å
pH_{zpc}	8.44	8.89

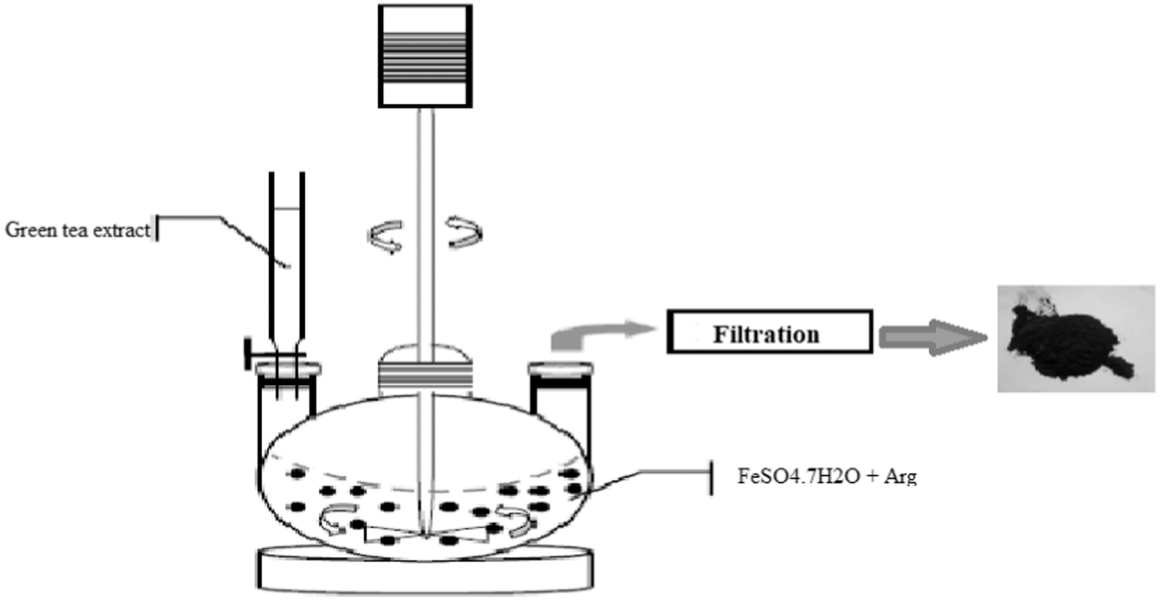

Fig. 1. : CnZVI synthesis scheme.

reported for nZVI loaded kaolinite, montmorillonite and Hangjin clays [12]. The total pore volume increased with introduction of nZVI from 0.11 to 0.28 $cm^3.g^{-1}$ signifying improved porosity structures.

The adsorption-desorption isotherms at 77 K for Arg and CnZVI are presented in Fig. 2. All the samples gave type IV isotherms, characteristic of microporous materials. The adsorption isotherms show adsorption-desorption hyteresis, indicating the presence of mesopores [29–31].

Fig. 3 shows the pore size distribution obtained from the adsorption isothermal curves for the powdered clay samples. Arg and CnZVI show mostly a unimodal pore distribution with peak around 27 Å and 17 Å respectively, thus symbolizing the presence of nanoparticles.

FTIR spectra of Arg and CnZVI are shown in Fig. 4. The absorption bands at 3688 and 3620 cm^{-1} observed on these adsorbents are attributed to the symmetrical vibrations of elongation of the free OH groups of the external surface and elongation vibrations of the internal OH groups, respectively [32–36]. Absorption bands located at 3323 and 1640 cm^{-1} on the IR spectrum of CnZVI indicates the presence of the O-H vibrations and the H-O-H deformation vibrations of adsorbed water molecules. The bands at 1116, 1114, 1104, and 1002 cm^{-1} are ascribed to the symmetric and asymmetric elongation vibrations of Si - O, Si-T (T = Si or Al) bonds. The observed vibration modes 910 and 907 cm^{-1} correspond to the vibration of the Al-OH bond [34,37,38]. They can also be due to the Fe-O-Si bond vibration modes when the sorbent contains a non-negligible amount of Fe_2O_3 [39]. The bands at 790 and 787 cm^{-1} are representative on the elongation vibrations of the Si-O bond of quartz [34,35]. The absorption bands located between 746 and 740 cm^{-1} correspond to the different vibration modes of the Si-O-Al IV bond (Al is in coordination IV) [38,40]. The bands at 529 and 401 cm^{-1} correspond to Si-O-T bond deformations (T, Si, Al, Fe) when the sorbent contains iron oxides in its chemical composition or receives iron during synthesis [39,41,42]. These bands can also be attributed to Si-O-Al VI (VI-coordinated Al) bonds [38,43].

Fig. 5 presents the thermal analysis (TGA in blue coupled to DSC in red) of the raw clay (Arg). This one highlights two endothermic phenomena corresponding to 63 °C and 507 °C. At 55 °C, the TGA thermogram shows a slight increase in mass which is translated on the DSC by an endothermic phenomenon related to the departure of water of hydration or hygroscopic. At 507 °C, the TGA presents a loss of mass of 9.2 % which is translated on the DSC by an endothermic phenomenon and corresponds to the dehydroxylation of the clay. This phenomenon corresponds to a departure of water of constitution and leads to the formation of metakaolinite according to Eq. (10):

$$Al_2O_3{\cdot}2SiO_2{\cdot}H_2O \rightarrow Al_2O_3{\cdot}2SiO_2 + H_2O \quad (10)$$

Compared to Fig. 5, the thermal analysis of the adsorbent CnZVI (Fig. 6) presents in addition to the endothermic phenomena, a succession of exothermic phenomena. Thus, between 100 °C and 200 °C, an endothermic phenomenon on the DSC curve which is accompanied by a very negligible loss of mass is observed, reflecting the departure of the water molecules absorbed during the synthesis of this adsorbent. The exothermic peak observed at 258 °C on the DSC curve can be attributed to the formation of lepidocrocite (γ-FeO(OH), thus confirming the incorporation of nanoparticles within the material during synthesis. As a result of this exothermic phenomenon, an endothermic peak located between 258 °C and 400 °C on the DSC curve is observed, which represents the dehydroxylation process of the lepidocrocite.

On the TGA thermogram, the process of formation and dehydroxylation of lepidocrocite is accompanied by a mass loss of about 2.70 %. At 505 °C, the TGA curve of the CnZVI adsorbent shows a significant loss of mass (about 8.47 %) which is translated on the DSC by an endothermic phenomenon and corresponds to dehydroxylation. This phenomenon corresponds to a departure of water of constitution and leads to the formation of metakaolinite as in the case of Arg. The peak observed at 698 °C on the DSC curve and the very low mass loss observed on the TGA (0.45 %) characterizes the structural reorganization of the adsorbent.

To better detect the impact of nZVI impregnation on the morphology and microstructural changes of the clay used as adsorbent, a surface micrograph was performed on the Arg and CnZVI adsorbent powders. The micrographs from the SEM analysis can be seen in Fig. 7.

For the Arg clay, the micrographs show layers tight on top of each other and a compact surface within which very small diameter pores are noticeable. The dark appearance of this surface would be due to the presence of minerals rich in silicon (SiO_2) and aluminum (Al_2O_3) oxides. Contrary to the Arg sample, the micrograph of the CnZVI adsorbent obtained with the same resolution (1 μm) shows the homogenous surface in which the volume and the size of the pores are more important. The observed white color aggregates are grouped in clusters of ordered particles with larger dark blocks. The strong whitish coloration observed on this one is due to the insertion of Fe-O nanoparticles in the polymeric networks of the starting kaolinite clay. It is essential to remark that, during the course of impregnation of iron nanoparticles, the reduction of iron II into iron zero leads to an opening of the pores within Arg. From the EDX analysis, an increase from 0.2 to 1.1 % in zero iron mass is realized.

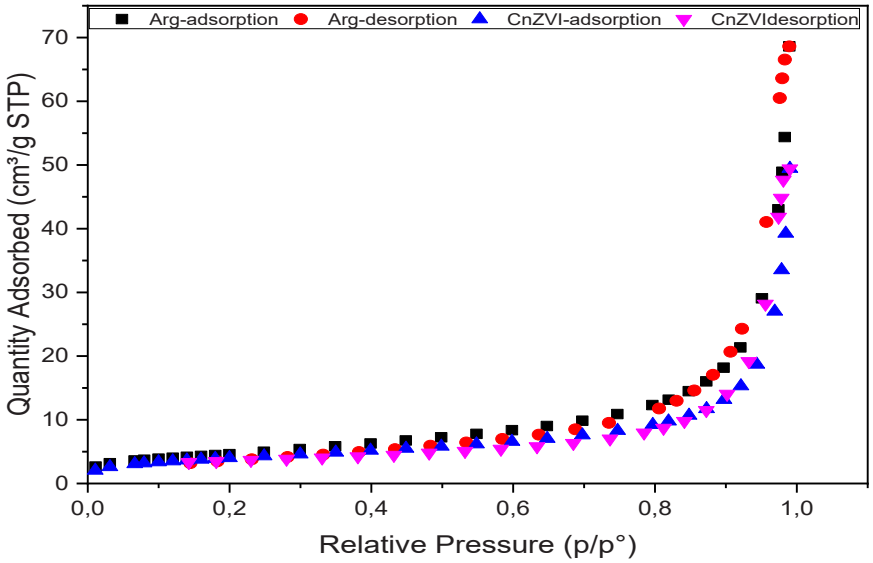

Fig. 2. : Adsorption-desorption isotherms of N_2 onto adsorbents.

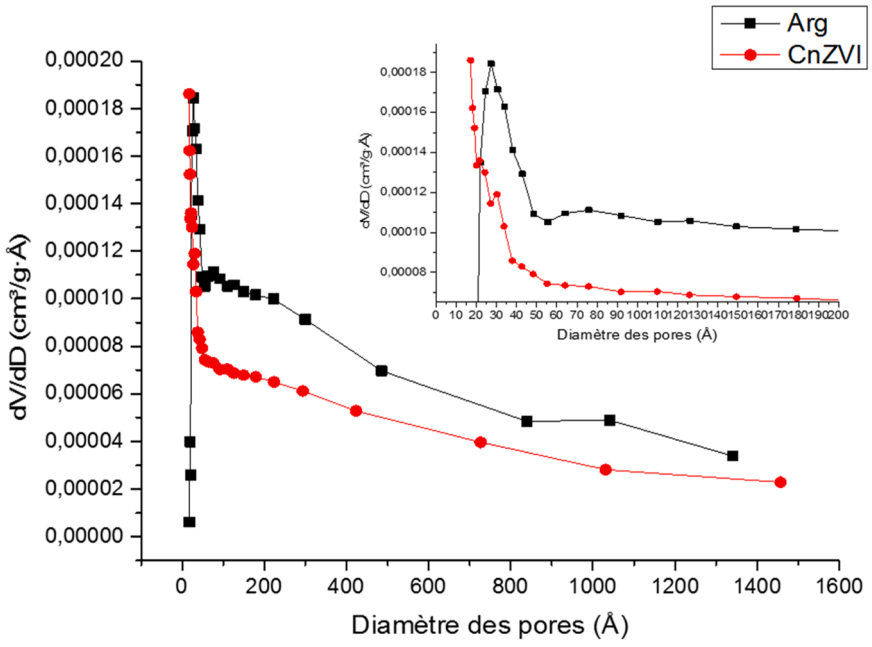

Fig. 3. Pore size distributions obtained from inversion of nitrogen at 77 K adsorption data for Arg and CnZVI.

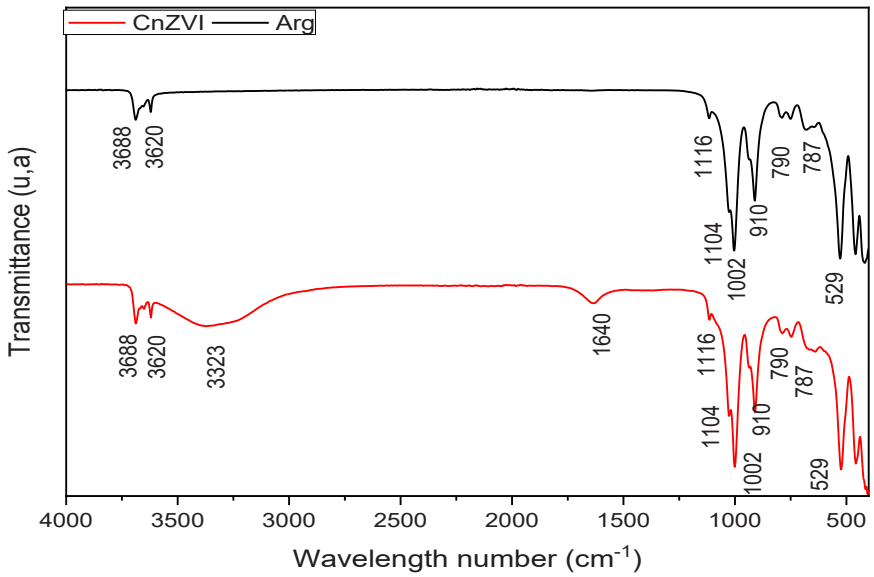

Fig. 4. : FTIR spectra of Arg and CnZVI.

3.2. Equilibrium studies

3.2.1. Effect of metal ions initial concentration

Fig. 8 represents the influence of different concentrations of Ni^{2+} ions on the equilibrium adsorption capacity. When the initial Ni^{2+} concentration is increased from 10 to 100 mgL^{-1}, the uptake capacity increased from 0.8012 to 8.361 mgg^{-1} and from 1.431 to 14.250 $mgg^{-1}$for Arg and CnZVI, respectively. This is due to the increase in mass gradient that serves as the driving force of the adsorbate molecules across the boundary to the adsorbent surface. This is also denoting existence of more energetically favorable binding sites for the uptake of additional Ni^{2+} ions.

3.2.2. Isothermal analysis

The adsorption isotherms of Arg and CnZVI are given in Fig. 9 and Fig. 10, respectively. Equilibrium data were modeled by three two-parameter isotherms, ie, Langmuir, Freundlich, and D-R isotherm equations and the related parameters are presented in Table 2. Based on the coefficient of determination, R^2, values (Table 2), the D-R model best predicted the pseudo-equilibrium adsorption data for the uptake of Ni^{2+} onto Arg with a maximum adsorption capacity of 8.47 mgg^{-1}. In contrast, the adsorption of Ni^{2+} onto Arg was best predicted by the Freundlich model implying multilayer adsorption phenomenon. The obtained 1/n value (1.894) signify weak interactions between Ni^{2+} and the CnZVI corresponding to physisorption mechanisms [44]. Based on the Langmuir model, the maximum adsorption capacity of CnZVI was 14.37 mgg^{-1}, representing 69.66 % increase in adsorption capacity. This is attributed to the increase in specific surface area improving accessibility to the active sites. However, the variance between the percent increase in surface area (~80 %) against increase in adsorption capacity (~69 %) denotes antagonistic effect between the surface chemistry and the textural properties. This is supported by the

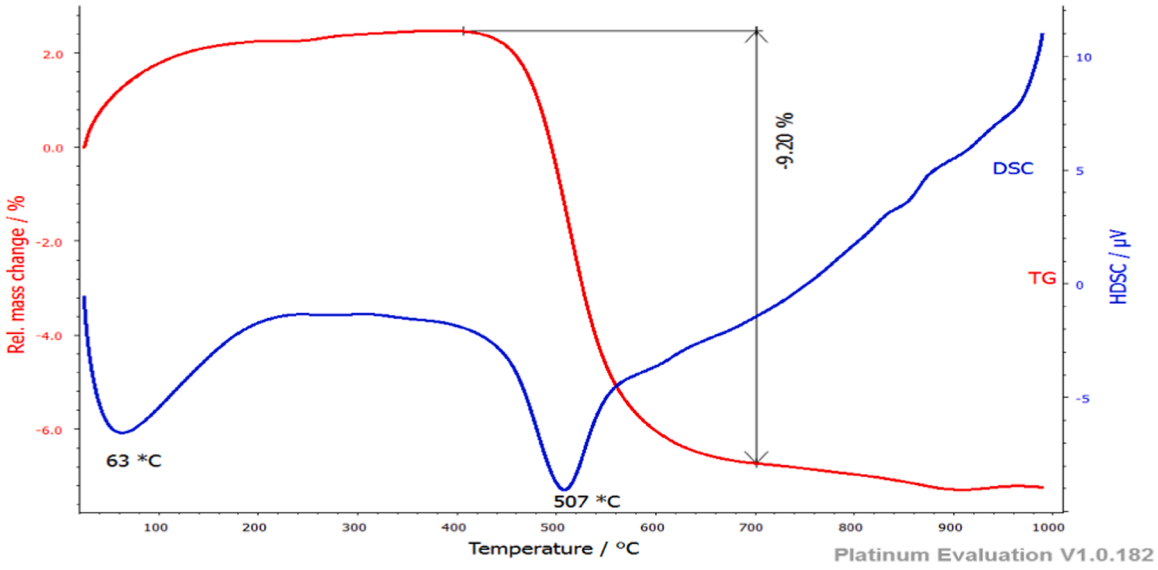

Fig. 5. : ATG/DSC curve of Arg.

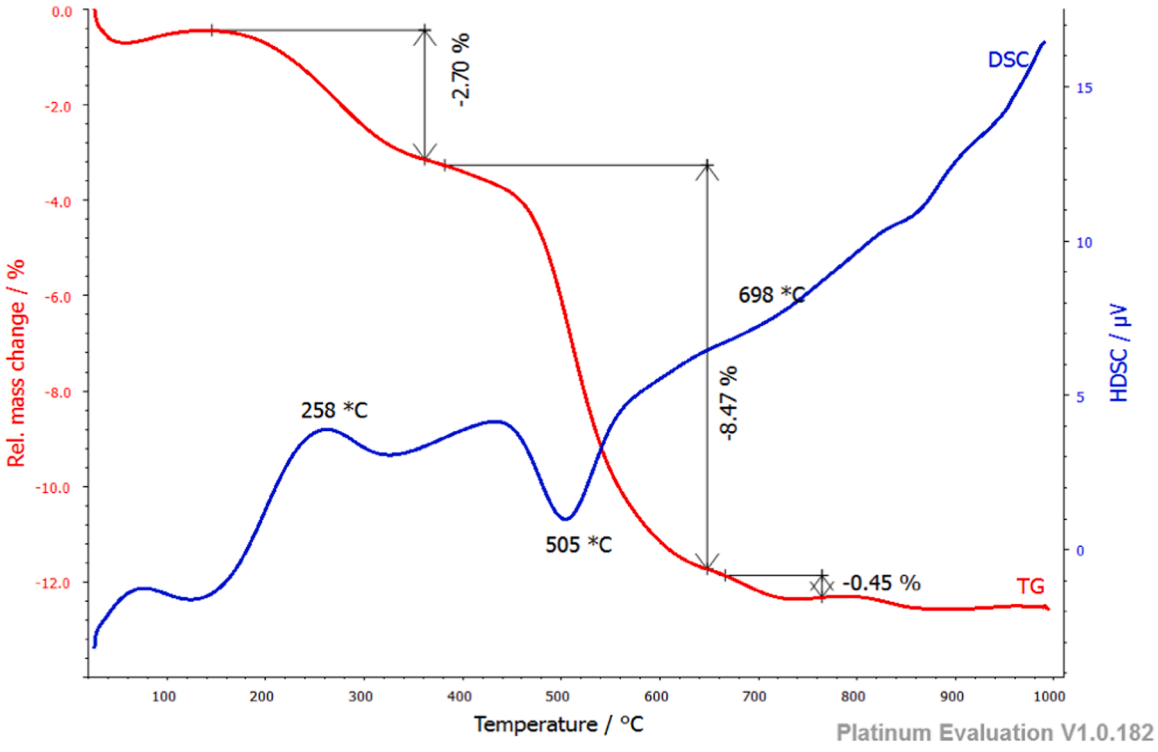

Fig. 6. : ATG/DSC curve of CnZVI.

Freundlich constant (K_F) values that denote higher adsorbate affinity in Arg relative to CnZVI (Table 2) [45]. According to Mishra and Tiwari [46], the apparent equilibrium constant (Ka), calculated as the product of q_m and K_L, obtained from the Langmuir isotherm, also provides an index of the relative affinity of the adsorbent toward the Ni^{2+} ions. However, this comparison could not be conclusively deduced since the Langmuir model did not adequately predict the pseudo-equilibrium adsorption data onto Arg. Overall, the incorporation of nZVI altered the surface chemistry in a way that increased the overall surface area but made the surface less specific for nickel ion adsorption.

Additionally, an increase in surface area might have resulted in a greater variety of active sites, some of which have lower affinity for nickel ions. While the number of adsorption sites in CnZVI increased, these sites may not be as effective as those on Arg, leading to a decrease in the overall affinity constant, K_F.

3.3. *Kinetics studies*

3.3.1. *Effect of contact time*

Fig. 11. illustrates the influence of contact time on the Ni^{2+} adsorption on Arg and CnZVI. Results show that the adsorption metal capacity increases progressively with time, until reaching a maximum value representing the membrane saturation. The high uptake rate in the first stage (during the first 20 min) is due to a high driving force, which

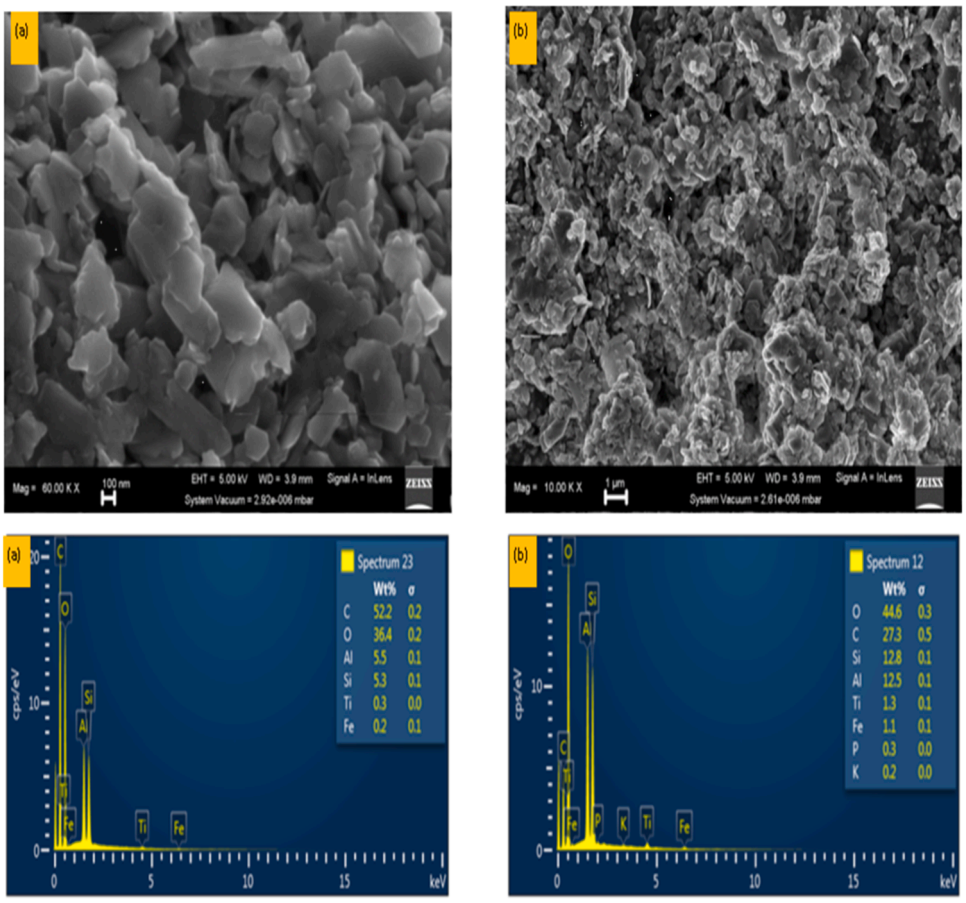

Fig. 7. : Micrograph of the surface and EDX of Arg(a) and CnZVI(b).

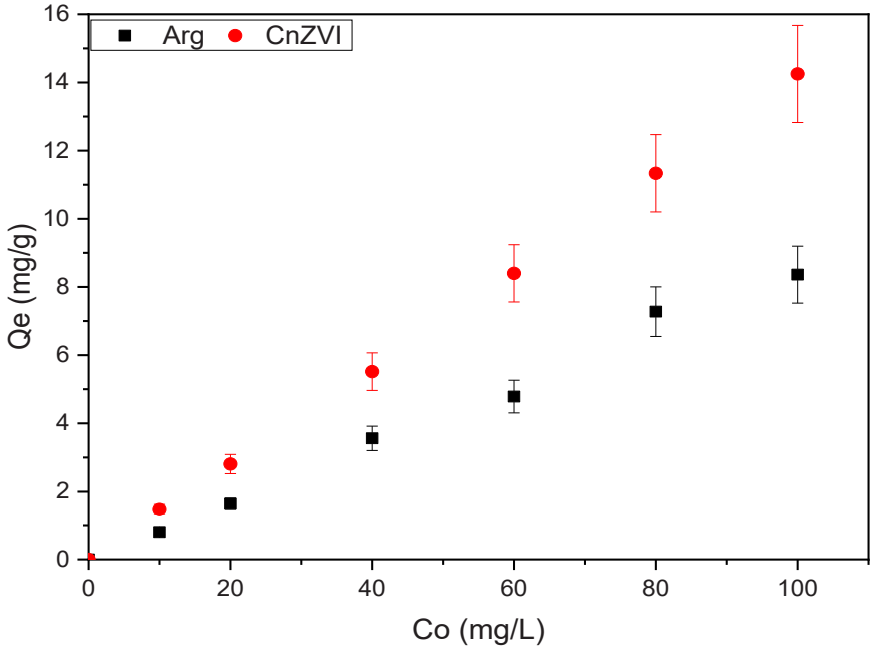

Fig. 8. Influence of initial Ni^{2+} concentration on adsorption capacity of Ni^{2+} using Arg and CnZVI (pH = 6.0, m = 0.2 g, V = 100 mL).

makes Ni^{2+} ions to transfer faster to the surface of the sorbents, along with the availability of a large number of vacant active binding sites [47]. The subsequent reduction is due to the reduced numbers of left active sites, inaccessibility to the inner pores and the repulsion between the adsorbed Ni^{2+} ions and those in the aqueous phase. It is clear that the pseudo-equilibrium adsorption capacity of CnZVI (14.25 mgg^{-1}) was higher than that of Arg 10.57 mgg^{-1}). Based on preliminary studies, 120 min was considered sufficient for attainment of pseudo-equilibrium

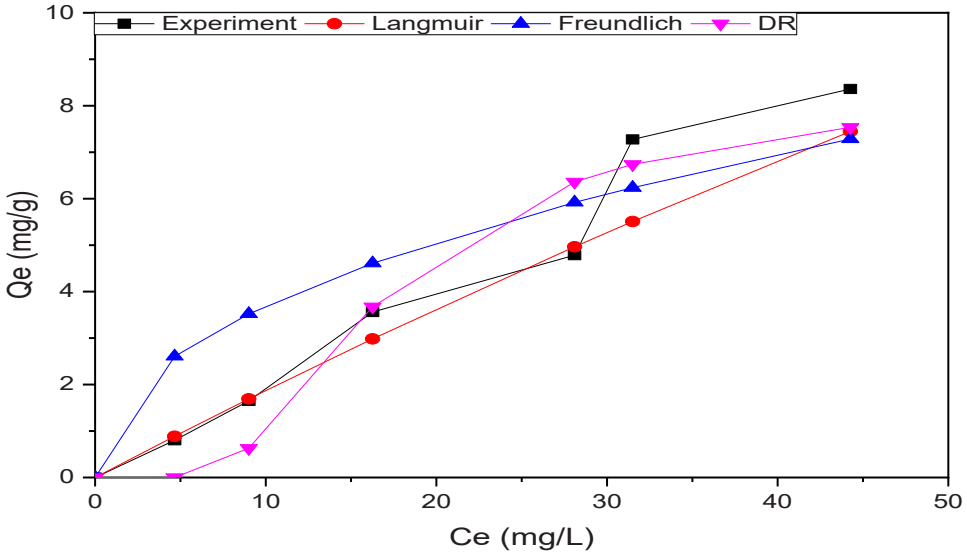

Fig. 9. Adsorption isotherms of Ni^{2+} on Arg.

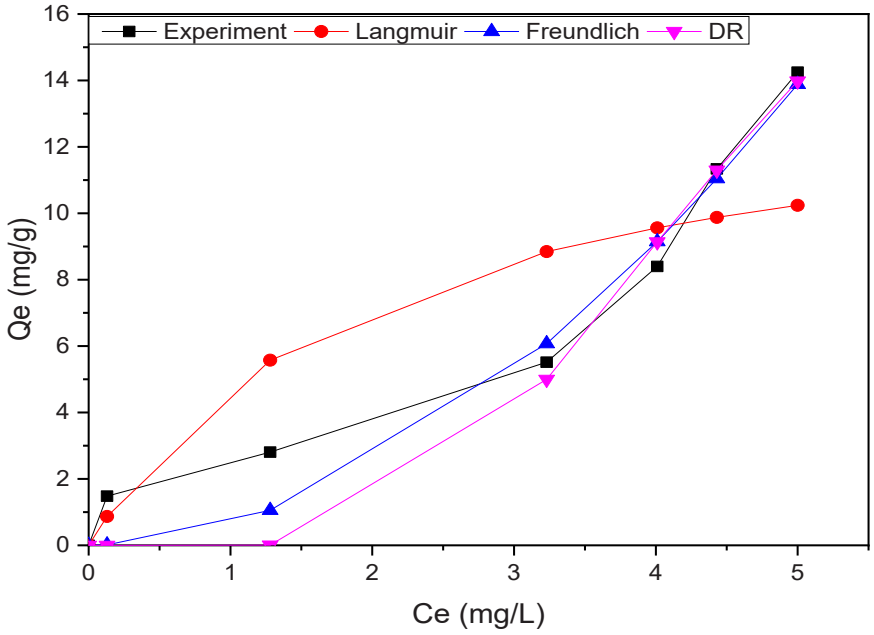

Fig. 10. Adsorption isotherms of Ni^{2+} on CnZVI.

for development of isothermal studies. The use of pseudo-equilibrium conditions to derive isotherms has been used in literature [48].

3.3.2. *Adsorption kinetics*

Three adsorption kinetic models are used to analyze the experimental data to know the adsorption rate and possible adsorption mechanism of Ni^{2+} ions on Arg and CnZVI. The results have been presented in Fig. 12. and Fig. 13, respectively. The parameters of the different kinetic models are grouped in Table 3.

Based on the coefficients of determination (R^2) values, the adsorption kinetics of Ni^{2+} on Arg was better described by the pseudo-first order (PFO) which indicates that physisorption is the rate-determining step [49]. The rate of change of the adsorbed solute with time is proportional to the saturation concentration difference and the amount of adsorbed solid with time, which is mainly applicable to the initial stage of an adsorption process. In the pseudo-first order parameters, the equilibrium adsorption capacity (q_e) value for CnZVI was higher than that obtained from Arg, implying that loading nZVI onto the unmodified clay surface actually increased the adsorption capacity for Ni^{2+}. The adsorption of Ni^{2+} on CnZVI was best described by the Elovich kinetic model (R^2 =0.996) implying that the adsorption behavior entailed a chemisorption-controlled phenomenon [50]. The results also indicate incorporation of nZVI increased the adsorption rate based on the rate constants. The shift from physisorption to chemisorption following coating with nZVI particles denote introduction of new adsorption sites of heterogeneous energies.

The adsorption densities of Arg and CnZVI relative to adsorbents applied in the sequestration Ni^{2+} ions from aqueous media are presented in Table 4. The adsorption capacities are observed to be comparable and superior to some of the materials reported in literature.

Table 5 shows the result of batch test involving the amount of heavy metals absorbed by CnZVI.

Table 2
Isotherm parameters on the adsorption of Ni^{2+}onto Arg and CnZVI.

Isotherm models	Arg	CnZVI
Langmuir model		
q_m (mgg^{-1})	10.846	14.377
K_L (Lmg^{-1})	0.003	0.495
Ka	0.032	7.117
R_L	0.745	0.019
^2_R	0.303	0.912
Freundlich model		
K_F (mgg^{-1}) $(mg/L)^{1/n}$	1.291	0.660
1/n	0.456	1.894
^2_R	0.748	0.948
Dubinin–Radushkevich model		
q_m (mgg^{-1})	8.474	33.232
$\beta(mol^2\ KJ^{-2})$	0.072	0.218
Ea ($KJ.mol^{-1}$)	2.635	1.514
^2_R	0.886	0.911

The adsorption capacities were in the order $Cu^{2+} > Pb^{2+} > Zn^{2+} > Ni^{2+} > Cd^{2+} > Hg^{2+}$. The sequence was attributed to a combination of several factors, including charge density, ionic radius, hydration energies and other specific interactions with the adsorbent. For instance, Cu^{2+} has a smaller ionic radius than other ions resulting to a comparatively high charge density. Consequently, Cu^{2+} exhibited strong interactions with adsorption sites resulting to the high maximum adsorption capacity. The relatively lower hydration energy of Zn^{2+} relative to Ni^{2+} could account for slightly higher adsorption for zinc. Whereas Cd^{2+} and Hg^{2+} have lower hydration energies, their large ionic radii are postulated to limit their uptake resulting to low adsorption capacity. The adsorption capacities are therefore a function of multiple drivers.

4. Conclusion

In this work, nanozerovalent iron (nZVI) supported clay hybrid was used as an efficient and inexpensive adsorbent for the removal of Ni^{2+}

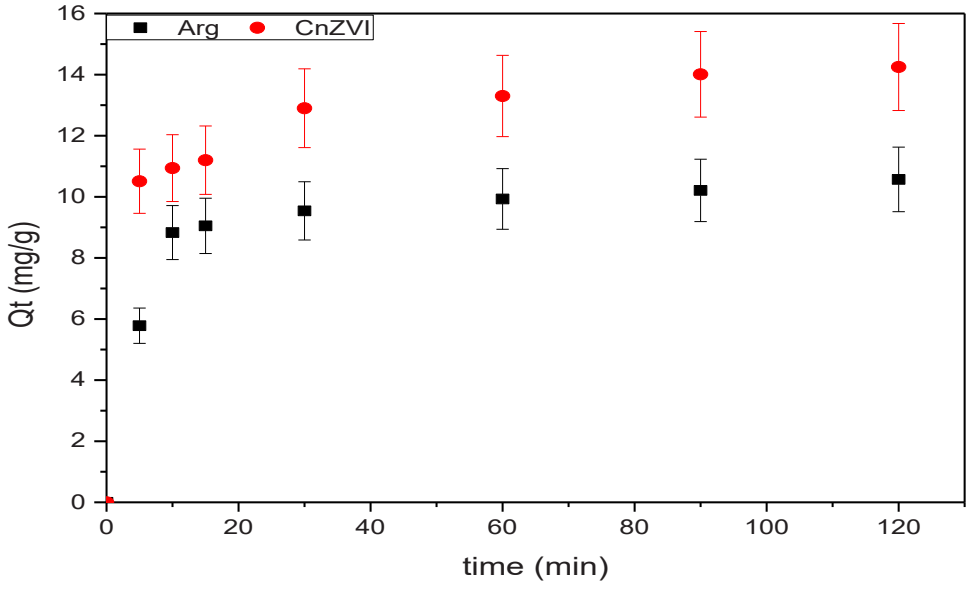

Fig. 11. : Influence of contact time on the uptake of Ni^{2+}ions onto Arg and CnZVI (C_0 = 100 $mg.L^{-1}$, pH= 6.0, m = 0.2 g, V = 30 mL).

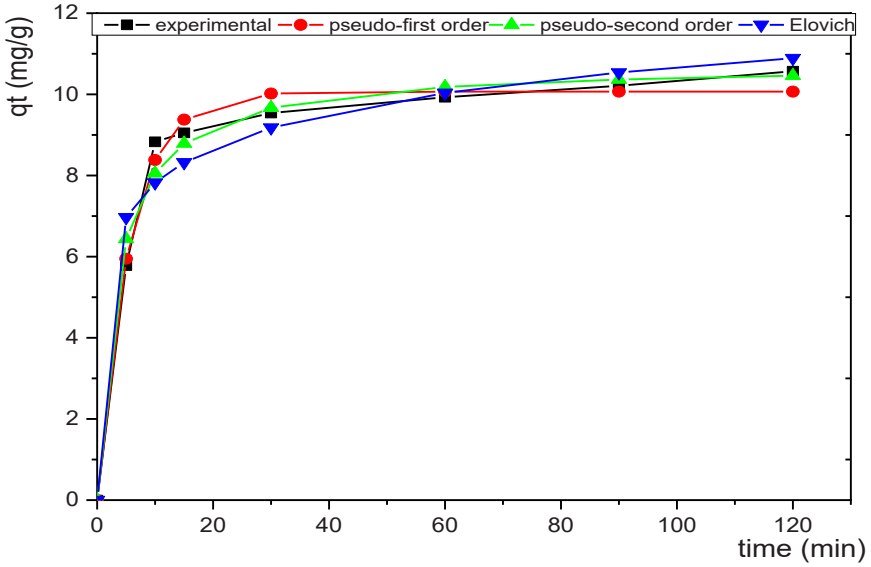

Fig. 12. Adsorption kinetic fit for the removal of Ni^{2+}ions by Arg (C_0 = 100mgL^{-1}, pH= 6.0, m = 0.2 g, V =100 mL).

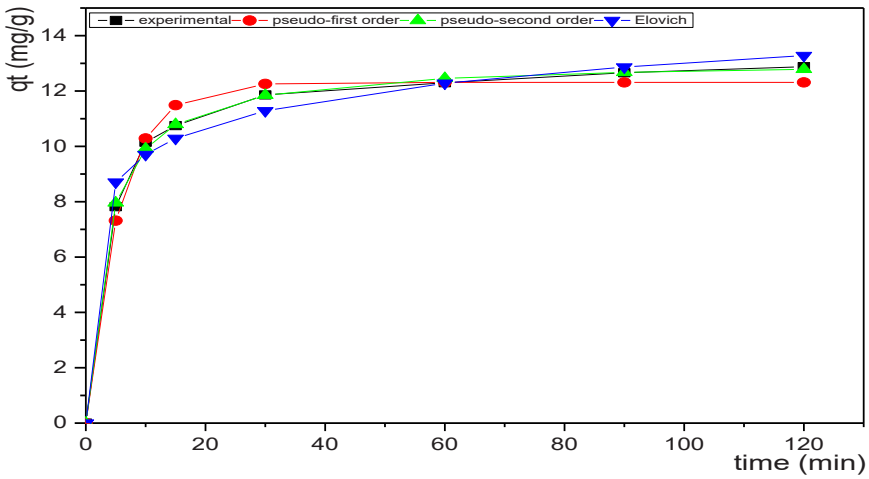

Fig. 13. Adsorption kinetic fit for the removal of Ni^{2+} ions by CnZVI (C_0 = 100mgL^{-1}, pH= 6.0, m = 0.2 g, V = 100 mL).

Table 3
Adsorption kinetic data for the removal of Ni^{2+}ions by Arg and CnZVI.

Adsorption kinetic model	Arg	CnZVI
$Q_{e,exp}$	8.361	14.250
Pseudo first-order		
Q_e (mgg^{-1})	10.066	13.131
K_1 (min^{-1})	0.178	0.255
^2_R	0.988	0.951
Pseudo second-order		
Q_e (mgg^{-1})	10.752	13.950
K_2 (gmg^{-1}min^{-1})	0.027	0.032
^2_R	0.986	0.984
Elovich kinetic model		
α (mgg^{-1}min^{-1})	0.192	0.272
β(gmg^{-1})	386.416	2280.524
^2_R	0.962	0.996

Table 4
A comparison of Ni^{2+} adsorption capacity of Arg and CnZVI with other adsorbents.

Adsorbents	Q_e (mg/g)	Reference
Rice husks	8.86	[51]
Halzenut shell	10.10	[52]
Fly ash	0.03	[53]
Protonated rice bran	46.51	[54]
Clinoptilolite	0.90	[55]
Banana peel	6.80	[56]
Row down seed	3.24	[57]
Arg	10.85	This study
CnZVI	14.38	This study

Table 5
Result of Batch Test using CnZVI.

Metals ions	Ni^{2+}	Cu^{2+}	Zn^{2+}	Hg^{2+}	Pb^{2+}	Cd^{2+}
Qe (mg/g)	14.38	65.20	20.95	11.23	48.25	12.23

ions from an aqueous solution. Incorporation of nZVI increased the specific surface area from 16.88 to 30.46 m^2/g, representing ~80 % increase. This translated to an increase in maximum adsorption capacity from 8.47 to 14.38 mg/g, representing ~69 % increase, for unmodified clay (Arg) and CnZVI, respectively. The increase in adsorption capacity with introduction of nZVI is due to increased surface area. The impregnation with nZVI introduction of new energetically unfavorable surfaces as denoted by the Freundlich constant (K_F). Faster kinetics correspond to a shorter residence time for CnZVI. The adsorption of Ni^{2+} is shown to be controlled by its high charge density that compensates for the antagonistic effect of hydration energies relative to other ions. The kinetic rates were best predicted by the pseudo-first-order and Elovich's equations for the Arg and CnZVI, respectively. CnZVI exhibited faster adsorption rates corresponding to shorter residence time. It is important to note that despite the fact that nZVI offers promising solutions for pollution control, rigorous assessments of the risks associated with its use are essential. Further studies are needed to better understand its environmental and health impacts to ensure safe and effective use.

CRediT authorship contribution statement

Charles Kede: Writing – original draft, Investigation. **Armand Tchakounte:** Writing – review & editing, Supervision, Resources, Funding acquisition, Conceptualization. **Joseph Dika:** Writing – review & editing, Supervision, Formal analysis. **Victor Shikuku:** Writing – review & editing, Methodology, Data curation. **Idriss Lenou:** Writing – review & editing, Methodology, Data curation.

Declaration of Competing Interest

The authors declare the following financial interests/personal relationships which may be considered as potential competing interests: Armand Tchakounte reports equipment, drugs, or supplies was provided by Tshwane University of Technology. If there are other authors, they declare that they have no known competing financial interests or personal relationships that could have appeared to influence the work reported in this paper.

Data availability

The authors confirm that the data supporting the findings of this study are available within the article.

References

[1] Mouni L, Djoudi M, Didier R, Abdelkrim B. Batch studies for the investigation of the sorption of the heavy metals Pb^{2+} and Zn^{2+} onto Amizour soil (Algeria). Geoderma 2009;154(1–2):30–5. https://doi.org/10.1016/j.geoderma.2009.09.007.
[2] Genchi G, Alessia C, Graziantonio L, Maria SS. Nickel: human health and environmental toxicology. Int J Environ Res Public Health 2020;17(679):1–21.
[3] Lalhruaitluanga H, Jayaram K, Prasad MNV, Kumar KK. Lead(II) adsorption from aqueous solutions by raw and activated charcoals of Melocanna baccifera Roxburgh (bamboo)-A comparative study. J Hazard Mater 2010;175(1–3):311–8. doi: 10.1016/j.jhazmat.2009.10.005.

[4] Sushil R, Manning B, Laurent C, Heechul C. Removal of Arsenic(III) from groundwater by nanoscale zero-valent iron. Environ Sci Technol 2005;39(5): 1291–8. https://doi.org/10.1021/es048991u.

[5] Elawwad A, Karam A, Zaher K. Using an algal photo-bioreactor as a polishing step for secondary treated wastewater. Pol J Environ Stud 2017;26(4). https://doi.org/10.15244/pjoes/68426).

[6] Badawi AK, Hassan R, Farouk M, Bakhoum ES, Salama RS. Optimizing the coagulation/flocculation process for the treatment of slaughterhouse and meat processing wastewater: experimental studies and pilot-scale proposal. Int J Environ Sci Technol 2024:1–16.

[7] Badawi AK, Salama RS, Mostafa MMM. Natural-based coagulants/flocculants as sustainable market-valued products for industrial wastewater treatment: a review of recent developments. RSC Adv 2023;13(28):19335–55. https://doi.org/10.1039/D3RA01999C.

[8] Tarekegn MM, Andualem MH, Dekebo AH. Nano zero valent iron (NZVI) particles for the removal of heavy metals (Cd^{2+}, Cu^{2+} and Pb^{2+}) from aqueous solutions. RSC Adv 2021;11(2021):18539–51. https://doi.org/10.1039/d1ra01427g.

[9] Okello VA, Masika OI, Shikuku VO. Reduction and degradation of paraoxon in water using zero-valent iron nanoparticles. Sustainability 2022;14(15). https://doi.org/10.3390/su14159451.

[10] Armand TN, Poumve HZ, Kede CM, Dika JM. Calcareous-support nanoscale zero-valent iron: new findings on adsorption of Cr (VI) in aqueous solution. J Appl Surf Interfaces 2019;6(1–3):9–17. https://doi.org/10.48442/IMIST.PRSM/jasi-v6i1-3.17461.

[11] Hoag EG, Collins JB, Holcomb JL, Hoag JR, Nadagouda N, Varma RS. Degradation of bromothymol blue by 'Greener' nano-scale zero-valent iron synthesized using tea polyphenols. J Mater Chem 2009;19:8671–7. https://doi.org/10.1039/b909148c.

[12] Li X, Zhao Y, Xi B, Mao X, Gong B, Li R, et al. Removal of nitrobenzene by immobilized nanoscale zero-valent iron: effect of clay support and efficiency optimization. Appl Surf Sci 2016. https://doi.org/10.1016/j.apsusc.2016.01.141.

[13] Uddin MK. A review on the adsorption of heavy metals by clay minerals, with special focus on the past decade. Chem Eng J 2017;308:438–62. https://doi.org/10.1016/j.cej.2016.09.029.

[14] Kede CM, Etoh MA, Ndibewu PP, Ngomo HM, Ghogomu PM. Equilibria and kinetic studies on the adsorption of cadmium onto cameroonian wetland clays. Br J Appl Sci Technol 2014;4(7):1071–88. https://doi.org/10.9734/bjast/2014/4299.

[15] Abbassi R, Kumar A, Kumar N, Huang S, Jaffe P. Modeling and optimization of dye removal using 'Green' Clay supported iron nano-particles. Ecol Eng 2013;61 (2013):366–70. https://doi.org/10.1016/j.ecoleng.2013.09.040.

[16] Odler I. The BET-specific surface area of hydrated Portland cement and related materials. Cem Concr Res 2003;33(12):2049–56. https://doi.org/10.1016/S0008-8846(03)00225-4.

[17] Wibowo N, Setyadhi L, Wibowo D, Setiawan J, Ismadji S. Adsorption of benzene and toluene from aqueous solutions onto activated carbon and its acid and heat treated forms: influence of surface chemistry on adsorption. J Hazard Mater 2007; 146(1-2):237–42. https://doi.org/10.1016/j.jhazmat.2006.12.011.

[18] Zyoud AH, Zubi A, Zyoud SH, Hilal MH, Zyoud S, Qamhieh N, et al. Kaolin-supported ZnO nanoparticle catalysts in self-sensitized tetracycline photodegradation: Zero-point charge and pH effects. Appl Clay Sci 2019;182: 105294. https://doi.org/10.1016/j.clay.2019.105294.

[19] Ehtisham M, Badawi AK, Khan AM, Khan RA, Ismail B. Exploring moisture adsorption on cobalt-doped ZnFe 2 O 4 for applications in atmospheric water harvesting. RSC Adv 2024;14(9):6165–77. https://doi.org/10.1039/d3ra08152d.

[20] Ho YS, McKay G. Pseudo-second order model for sorption processes. Process Biochem 1999;34:451–65. https://doi.org/10.1021/acs.oprd.7b00090.

[21] Ho Y. Review of second-order models for adsorption systems. J Hazard Mater 2006; 136(3):681–9. https://doi.org/10.1016/j.jhazmat.2005.12.043.

[22] Elovich SYu, Larionov OG. Theory of adsorption from solutions of non-electrolytes on solid (I) equation adsorption from solutions and the analysis of its simplest form, (II) verification of the equation of adsorption isotherm from solution, Institute of Physical Chemistry. Acad Sci USSR 1962;2:298. 203.

[23] Sidjou AS, Armand T, Tome S, Kede C, Dika MJ. Use of Rice Husk Ash as a Potent Adsorbent of Malachite Green: Kinetic and Equilibrium Studies 2022;4(1):55–63. https://doi.org/10.48402/IMIST.PRSM/jasab-v4i1.31846.

[24] Lakhdhar I, Belosinschi D, Mangin P, Chabot B. Development of a bio-based sorbent media for the removal of nickel ions from aqueous solutions. J Environ Chem Eng 2016;4(3):3159–69. https://doi.org/10.1016/j.jece.2016.06.026.

[25] Langmuir I. The constitution and fundamental properties of solids and liquids. Part II.-liquids. J Frankl Inst 1917;184(5):2221–95. https://doi.org/10.1016/s0016-0032(17)90088-2.

[26] Freundlich Herbert. Über die adsorption in Lösungen. Z Fur Physlkalishe Chem 1907;57(4):385–470. https://doi.org/10.1515/zpch-1907-5723.

[27] Dubinin MM. Generalization of the Theory of Volume Filling of Micropores to Nonhomogeneous Microporous Structures 1985;23(4):373–80. https://doi.org/10.1016/0008-6223(85)90029-6.

[28] Shikuku VO, Mishra T. Adsorption isotherm modeling for methylene blue removal onto magnetic kaolinite clay: a comparison of two-parameter isotherms. Appl Water Sci 2021;11:103. https://doi.org/10.1007/s13201-021-01440-2.

[29] Hernández-montoya, Pérez-cruz VMA, Mendoza-castillo DI, Moreno-virgen MR. Competitive adsorption of dyes and heavy metals on zeolitic structures. J Environ Manag 2013;116:213–21. https://doi.org/10.1016/j.jenvman.2012.12.010.

[30] Medhat A, El-Maghrabi HH, Abdelghany A, Abdel Menem NM, Raynaud P, Moustafa YM, et al. Efficiently activated carbons from corn cob for methylene blue adsorption. Appl Surf Sci Adv 2021;3:100037. https://doi.org/10.1016/j.apsadv.2020.100037.

[31] Nada AA, Bekheet MF, Roualdes S, Gurlo A, Ayral A. Functionalization of MCM-41 with titanium oxynitride deposited via PECVD for enhanced removal of methylene blue. J Mol Liq 2019;274:505–15. https://doi.org/10.1016/j.molliq.2018.10.154.

[32] Kakali G, Perraki T, Tsivilis S, Badogiannis E. Thermal treatment of kaolin: the effect of mineralogy on the pozzolanic activity. Appl Clay Sci 2001;20(1-2):73–80. https://doi.org/10.1016/S0169-1317(01)00040-0.

[33] Hilal N, Al-Zoubi H, Mohammad A, Darwish N. Nanofiltration of highly concentrated salt solutions up to seawater salinity. Desalination 2005;184(1-3): 315–26. https://doi.org/10.1016/j.desal.2005.02.062.

[34] Kenne Diffo BB, Elimbi A, Cyr M, Dika Manga J, Tchakoute KH. Effect of the rate of calcination of kaolin on the properties of metakaolin-based geopolymers. J Asian Ceram Soc 2015;3(1):130–8. https://doi.org/10.1016/j.jascer.2014.12.003.

[35] Rehan M, Nada AA, Khattab TA, Abdelwahed NA, El-Kheir AAA. Development of multifunctional polyacrylonitrile/silver nanocomposite films: antimicrobial activity, catalytic activity, electrical conductivity, UV protection and SERS-active sensor. J Mater Res Technol 2020;9(4):9380–94. https://doi.org/10.1016/j.jmrt.2020.05.079.

[36] Salama RS, Gouda MS, Aboud MFA, Alshorifi FT, El-Hallag AA, Badawi AK. Synthesis and characterization of magnesium ferrite-activated carbon composites derived from orange peels for enhanced supercapacitor performance. Sci Rep 2024; 14(1):8223. https://doi.org/10.1038/s41598-024-54942-9.

[37] Abi Younes P, Sayegh S, Nada AA, Weber M, Iatsunskyi I, Coy E, et al. Elaboration of porous alumina nanofibers by electrospinning and molecular layer deposition for organic pollutant removal. Colloids Surf A Physicochem Eng Asp 2021;628: 127274. https://doi.org/10.1016/j.colsurfa.2021.127274.

[38] Saikia B, Parthasarathy G. Fourier transform infrared spectroscopic characterization of kaolinite from Assam and Meghalaya, Northeastern India. J Mod Phys 2010;1(4):206–10. https://doi.org/10.4236/jmp.2010.14031.

[39] Missota Priso Dickson B, Dika Manga J, Pougnong TE, et al. Effects of kinetic parameters on initial setting time, microstructure and mechanical strength of volcanic ash-based phosphate inorganic polymers. Silicon 2022;14:3693–705. https://doi.org/10.1007/s12633-021-01140-1.

[40] Pearlin Kiruba U, Senthil Kumar P, Sangita Gayatri K, Shahul Hameed S, Sindhuja M, Prabhakaran C. Study of adsorption kinetic, mechanism, isotherm, thermodynamic, and design models for Cu(II) ions on sulfuric acid-modified Eucalyptus seeds: temperature effect. Desalin Water Treat 2015;56(11):2948–65. https://doi.org/10.1080/19443994.2014.966279.

[41] Tchakouté HK, Rüscher CH, Kong S, Kamseu E, Leonelli C. Geopolymer binders from metakaolin using sodium waterglass from waste glass and rice husk ash as alternative activators: a comparative study. Constr Build Mater 2016;114:276–89. https://doi.org/10.1016/j.conbuildmat.2016.03.184.

[42] Bich C, Ambroise J, Péra J. Influence of degree of dehydroxylation on the pozzolanic activity of metakaolin. Appl Clay Sci 2009;44(3-4):194–200. https://doi.org/10.1016/j.clay.2009.01.014.

[43] Kaze RC, Beleuk à Moungam LM, Cannio M, Rosa R, Kamseu E, Melo UC, et al. Microstructure and engineering properties of Fe2O3(FeO)-Al2O3-SiO2 based geopolymer composites. J Clean Prod 2018;199:849–59. https://doi.org/10.1016/j.jclepro.2018.07.171.

[44] Jemutai-Kimosop S, Orata F, Shikuku VO, Okello VA, Getenga ZM. Insights on adsorption of carbamazepine onto iron oxide modified diatomaceous earth: Kinetics, isotherms, thermodynamics, and mechanisms. Environ Res 2019;180: 108898. https://doi.org/10.1016/j.envres.2019.108898.

[45] Luttah I, Onunga DO, Shikuku VO, Otieno B, Kowenje CO. Removal of endosulfan from water by municipal waste incineration fly ash-based geopolymers: adsorption kinetics, isotherms, and thermodynamics. Front Environ Chem 2023;4:1164372. https://doi.org/10.3389/fenvc.2023.1164372.

[46] Mishra T, Tiwari S. Studies on sorption properties of zeolite derived from Indian fly ash. J Hazard Mater 2006;137(1):299–303. https://doi.org/10.1016/j.jhazmat.2006.02.004.

[47] ZHOU YF, HAYNES RJ. Sorption of heavy metals by inorganic and organic components of solid wastes: significance to use of wastes as low-cost adsorbents and immobilizing agents. Crit Rev Environ Sci Technol 2010;40(11):909–77. https://doi.org/10.1080/10643380802586857.

[48] Das R, Mukherjee A, Sinha I, et al. Synthesis of potential bio-adsorbent from Indian Neem leaves (Azadirachta indica) and its optimization for malachite green dye removal from industrial wastes using response surface methodology: kinetics, isotherms and thermodynamic studies. Appl Water Sci 2020;10:117. https://doi.org/10.1007/s13201-020-01184-5.

[49] Aliabadi M, Irani M, Ismaeili J, Piri H, Parnian MJ. Electrospun nanofiber membrane of PEO/Chitosan for the adsorption of nickel, cadmium, lead and copper ions from aqueous solution. Chem Eng J 2013;220:237–43. https://doi.org/10.1016/j.cej.2013.01.021.

[50] Wu F, Tseng R, Juang R. Characteristics of Elovich equation used for the analysis of adsorption kinetics in dye-chitosan systems. Chem Eng J 2009;150(2-3):366–73. https://doi.org/10.1016/j.cej.2009.01.014.

[51] Bansal M, Singh D, Garg VK, Rose P. Use of agricultural waste for the removal of nickel ions from aqueous solutions: equilibrium and kinetics studies. Int J Civ Environ Eng 2009;3(3):174–80. https://doi.org/10.5281/zenodo.1075328.

[52] Demirbaş E, Kobya M, Öncel S, Şencan S. Removal of Ni(II) from aqueous solution by adsorption onto hazelnut shell activated carbon: equilibrium studies. Bioresour Technol 2002;84(3):291–3. https://doi.org/10.1016/S0960-8524(02)00052-4.

[53] Rao M, Parwate A, Bhole A. Removal of Cr^{6+} and Ni^{2+} from aqueous solution using bagasse and fly ash. Waste Manag 2002;22(7):821–30. https://doi.org/10.1016/S0956-053X(02)00011-9.

[54] Zafar MN, Nadeem R, Hanif MA. Biosorption of nickel from protonated rice bran. J Hazard Mater 2007;143(1-2):478–85. https://doi.org/10.1016/j.jhazmat.2006.09.055.
[55] Ouki S, Kavannagh M. Treatment of metals-contaminated wastewaters by use of natural zeolites. Water Sci Technol 1998;39(10-11):115–22. https://doi.org/10.1016/S0273-1223(99)00260-7.
[56] Annadural G, Juang RS, Lee DJ. Adsorption of heavy metals from water using banana and orange peels. Water Sci Technol 2003;47(1):185–90.
[57] El-Sadaawy M, Abdelwahab O. Adsorptive removal of nickel from aqueous solutions by activated carbons from doum seed (Hyphaenethebaica) coat. Alex Eng J 2014;53(2):399–408. https://doi.org/10.1016/j.aej.2014.03.014.